Pergamon

Geochimica et Cosmochimica Acta, Vol. 58, No. 8, pp. 1937–1949, 1994

0016-7037/94 $6.00 + .00

A $CaAl_4O_7$-bearing refractory spherule from Murchison: Evidence for very high-temperature melting in the solar nebula

S. B. SIMON,[1] S. YONEDA,[1] L. GROSSMAN,[1,2] and A. M. DAVIS[2]

[1]Department of the Geophysical Sciences, 5734 South Ellis Avenue, The University of Chicago, Chicago, IL 60637, USA
[2]Enrico Fermi Institute, 5640 South Ellis Avenue, The University of Chicago, Chicago, IL 60637, USA

(*Received July* 21, 1993; *accepted in revised form November* 30, 1993)

Abstract—We have recovered a unique refractory spherule, B6, from the Murchison C2 chondrite. Approximately 170 μm in diameter, it is concentrically zoned, with an outer rim sequence, from outermost to innermost, of aluminous diopside (10 μm thick), anorthite (3 μm), and melilite (3 μm). Inside the melilite layer is a 7 μm-thick, nearly pure layer of spinel. Inward from this layer is a 20-μm wide zone of hibonite laths enclosed in spinel. Inward from this zone, at the core of the inclusion, is $CaAl_4O_7$ + perovskite. This is the first reported occurrence of $CaAl_4O_7$ in a Murchison inclusion. The sequence of mineral assemblages from the spinel shell inward parallels that expected for crystallization of a melt with the composition of this spherule: 73.2 wt% Al_2O_3; 17.7% MgO; 6.5% CaO; and 2.5% TiO_2. From the bulk composition of the inclusion, distribution of phases, and spherical shape, we conclude that the oxide phases in it, including spinel, crystallized from a liquid. From calculated phase relations in the system Al_2O_3–MgO–CaO, we infer a melting temperature of ~2100°C, the highest ever inferred for a refractory inclusion. Evidence of a high-temperature history is also seen in the spinel, which, unlike that in most CAIs, contains 1–2 mol% excess Al_2O_3 relative to stoichiometric $MgAl_2O_4$. At this temperature, B6 should have been grossly out of equilibrium (by ~600°C) with a gas of solar composition at 10^{-3} atm, but no evidence of evaporative loss is seen. The inclusion has a Group II REE pattern and a normal magnesium isotopic composition. The latter observation requires a very brief cooling time, on the order of several seconds. This is consistent with cooling rates calculated for a liquid spherule of the size and composition of B6 undergoing radiative cooling in the solar nebula and constrains the heating mechanism to a small-scale event. We propose the following sequence for the formation of B6: condensation of solid precursors; melting of those precursors in a hypervelocity collision which caused heating of the melt to ~2100°C; rapid formation of the spinel shell, preventing evaporation of the melt; fractional crystallization of the melt; and addition, probably by condensation, of the silicate layers. Corundum and $CaAl_4O_7$ are very rarely found in Murchison CAIs. Apparently, most early formed, corundum-rich condensates continued to react with the solar nebula until hibonite, perovskite, and spinel had condensed, forming aggregates which, when melted, gave rise to liquids too rich in TiO_2, MgO, and CaO to yield corundum or $CaAl_4O_7$ upon cooling.

INTRODUCTION

CM2 CARBONACEOUS chondrites contain an important suite of refractory inclusions that are distinct from those in CV3 chondrites in that they consist of oxide phases, such as spinel, hibonite, and perovskite, rather than the silicates, such as melilite and fassaite, that characterize the well-documented Type A and Type B inclusions of CV3 chondrites (e.g., GROSSMAN, 1980). Whereas the Type B inclusions are thought to have crystallized from a partially molten state after reaching maximum temperatures of approximately 1400°C (STOLPER and PAQUE, 1986), the oxide-rich inclusions from CM2 chondrites are believed to have formed at even higher temperatures. For example, temperatures of at least 1550°C are indicated for some spinel-hibonite spherules from Murchison, assuming that the hibonite in them was completely molten and the spinel was not (MACPHERSON et al., 1983). If the spinel in these inclusions were even partially molten as well, even higher liquidus temperatures would be indicated. We have recovered from Murchison a spinel-, hibonite-, $CaAl_4O_7$-, perovskite-bearing spherule which appears to have been almost completely molten, requiring exposure to the highest temperature yet inferred for any refractory inclusion (BAR-MATTHEWS et al., 1982; MACPHERSON et al., 1984a). This is also the first reported occurrence of $CaAl_4O_7$ in a Murchison inclusion. Some preliminary results of this study were reported by SIMON et al. (1993a,b) and YONEDA et al. (1993).

ANALYTICAL METHODS

Sample Preparation, Scanning Electron Microscopy, and Electron Probe Microanalysis

Several chips of the Murchison CM2 carbonaceous chondrite, totalling approximately 18g, were disaggregated using the freeze-thaw method described by MACPHERSON et al. (1980). Objects that were blue to gray in color (and thus most likely to contain hibonite or corundum) were hand-picked under a binocular microscope from the densest fraction obtained ($\rho > 3.50$). One of these objects, numbered M92B6 (B6 hereafter), is the subject of this report. It was a nearly complete spherule, with a small piece missing. Using stainless steel dental tools, we broke it into two pieces, taking the smaller one for a thin section and the other, weighing 3.63 μg, for instrumental neutron activation analysis (INAA). The thin section was examined with a JEOL JSM-35 scanning electron microscope, equipped with a Kevex energy-dispersive X-ray system. Quantitative wavelength-dispersive analyses were performed with a fully automated Cameca SX-50 electron microprobe. Samples were analyzed at 15 kV with a beam current of 40 nA. The beam current and counting times were

higher than are routinely used, in order to obtain improved counting statistics. For the spinel analyses, counting times of 50 s for Mg and 20 s for Al were used, giving 2σ uncertainties due to counting statistics of 0.4% of the amount present for both Mg and Al. These elements were analyzed with the same spectrometer in order to avoid bias due to specimen tilt (for example, toward a spectrometer used for Al and away from one used for Mg). Synthetic crystals of stoichiometric $MgAl_2O_4$ were used as a standard and, as a check, were analyzed periodically throughout the run. For analyses of $CaAl_4O_7$, counting times of 30 s for Ca and 10 s for Al were used, yielding relative 2σ uncertainties of 0.8 and 0.5%, respectively. Background count rates were measured at offsets below and above each peak position for a total counting time equal to that used for the peak. Data were reduced via the modified ZAF correction procedure PAP (POUCHOU and PICHOIR, 1984).

Instrumental Neutron Activation Analysis

Bulk major, minor, and trace element abundances were determined by INAA, using methods quite similar to those described by DAVIS et al. (1982) and SYLVESTER et al. (1993). Magnesium, Al, Ti, Mn, and V were determined via rabbit (short) irradiation; Ca, Fe, and the trace elements by a long irradiation. Silicon was determined by difference from calculated oxide totals. The sample was irradiated at the University of Missouri Research Reactor along with other samples. The results for those samples, and the precise analytical conditions and methods used will be discussed in detail elsewhere (YONEDA et al., 1994).

Ion Microprobe Analysis

Trace element and magnesium isotopic analyses were obtained using the University of Chicago AEI IM-20 ion microprobe. The analytical techniques used are similar to those described in HINTON et al. (1988), DAVIS et al. (1991), SIMON et al. (1991), and MACPHERSON and DAVIS (1994). Analytical methods for magnesium isotopic analyses are given in HINTON and BISCHOFF (1984). The ion microprobe spot size was 15 μm for trace element analyses and 8 μm for isotopic analyses. Magnesium isotopic data were normalized to the data of CATANZARO et al. (1966).

All ion microprobe analysis spots are mixtures of phases, so the standard used for each spot depended on the major phase contributing to the analysis. Ca-normalized trace element ion yields for silicates were used for the pyroxene-anorthite rim, hibonite yields for the spinel-hibonite spot, and perovskite yields for the spots consisting of spinel + hibonite + perovskite and $CaAl_4O_7$ + perovskite. In the magnesium isotopic analysis of $CaAl_4O_7$, ~90% of the Mg signal is due to adjacent spinel-rich areas, so the same Al/Mg sensitivity factor ratio was used for this analysis as for spinel and hibonite.

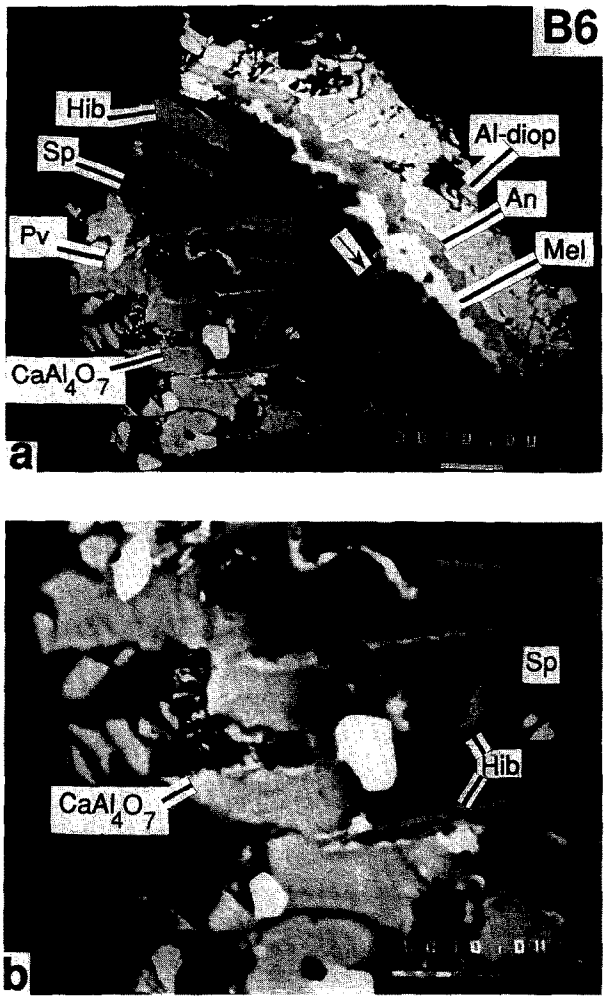

FIG. 1. (a) Backscattered electron image of B6. The section is a roughly pie-slice-shaped piece of a spherule, with aluminous diopside (Al-diop) on the outside and $CaAl_4O_7$ in the core. The arrow points to a spray of hibonite laths. Other abbreviations: Pv: perovskite; Sp: spinel; Hib: hibonite; Mel: melilite; An: anorthite. Scale bar is 10 μm. (b) Higher-magnification view of B6, showing the irregular $CaAl_4O_7$-spinel contact, and hibonite laths, some corroded, which extend from spinel into the $CaAl_4O_7$. Abbreviations as in (a). Scale bar is 10 μm.

RESULTS

Petrographic Description of B6

The sample studied in thin section is a roughly pie-slice-shaped fragment of the original spherule. Figure 1a is a backscattered electron image of the section. It shows that B6 is a concentrically zoned object, with a silicate rim sequence, from outermost to innermost, of aluminous diopside (10 μm thick), anorthite (3 μm), and melilite (3 μm). The same sequence of phases was observed by MACPHERSON et al. (1983) in the rim of the melilite-rich inclusion MUM-1 from Murchison, but not on any hibonite-spinel spherules. As in MUM-1, the spinel-melilite, melilite-anorthite, and anorthite-pyroxene contacts in B6 appear embayed and irregular, rather than smooth.

Inside the melilite layer in B6 is a thin (~7 μm) layer composed almost entirely of spinel. Inward from the spinel layer is a zone of hibonite + spinel, in which pale blue hibonite laths 1–4 μm across and up to 10 μm long are enclosed in spinel. The spinel-hibonite zone has several large cavities that appear, in some cases, to cross spinel-hibonite grain boundaries. It is not clear whether these cavities are primary (due to shrinkage during cooling), secondary (due to nebular or parent body alteration), or were caused by plucking during sample preparation. Many of the laths are radially oriented, including a small spray of crystals, indicated by the arrow in Fig. 1a, that diverges inward from the spinel-melilite contact. This texture is like that observed in other hibonite-spinel spherules (MACDOUGALL, 1981; MACPHERSON et al., 1983). Inward from the hibonite-spinel zone, presumably forming the core of the inclusion, is $CaAl_4O_7$, which encloses anhedral grains of perovskite that are 2–5 μm across. The $CaAl_4O_7$ crystals are also anhedral and are ~10 μm across. This is the first report of $CaAl_4O_7$ in a Murchison inclusion, although

this phase has been reported in inclusions from other carbonaceous chondrites (e.g., MICHEL-LÉVY et al., 1982; PAQUE, 1987; GROSSMAN et al., 1988; BISCHOFF et al., 1993a). As shown in Fig. 1b, there are cavities in the $CaAl_4O_7$, the contact between the $CaAl_4O_7$ and the spinel-hibonite zone is irregular, and some of the hibonite laths, such as the large one indicated in Fig. 1b, protrude into the $CaAl_4O_7$. This lath appears to be quite corroded, like one of the other large laths in Fig. 1b but unlike the hibonite in other hibonite-spinel spherules (e.g., MACPHERSON et al., 1983; IRELAND, 1988).

Mineral Chemistry

Spinel

Spinel is nearly pure $MgAl_2O_4$, with less than 0.2 wt% of each of Cr_2O_3, FeO, V_2O_3, and TiO_2. Representative electron probe analyses of spinel in B6 and other Murchison inclusions are given in Table 1. Analyses of spinel in B6 and other CAIs from Murchison and Allende, and of our spinel standard are plotted in Fig. 2. All analyses shown were collected on the same day under the same conditions. From the average of seven analyses of the pure, stoichiometric $MgAl_2O_4$ spinel standard, we determined that the analyses had 0.004 too many Mg-site cations and 0.004 too few Al-site cations per four oxygen ions. The data in Table 1 are uncorrected, but we applied this correction to all the analyses plotted in Fig. 2, so that the average standard analysis now plots at $MgAl_2O_4$, the intersection of the lines in Fig. 2. The spread of values of the spinel standard about this point is a measure of the precision of the analyses. In spite of the presence of several cations (e.g., Cr, V, and Ti) which substitute for Al, the average of all thirteen B6 spinel analyses contains more than 2 Al ions alone per four oxygen ions and, as Fig. 2 shows, has 2.006–2.015 Al-site ions per four oxygen ions. It also has less than 0.990 Mg + Fe + Ca ions per four oxygen ions. As shown in Table 1 and illustrated by Fig. 2, this spinel is distinct from that in other Murchison CAIs, which have >0.990 Mg + Fe + Ca and ≤2.004 Al-site ions per four oxygen ions. The difference in composition between the spinel in B6 and that in the other CAIs is much larger than the uncertainty due to counting statistics, the spread of values of the $MgAl_2O_4$ standard around the stoichiometric value, and the correction for systematic error applied to the data. This difference can be explained by solid solution of Al_2O_3 in the B6 spinel, which has the effect of decreasing the number of Mg + other cations and increasing the number of Al + other cations per four oxygen ions. For example, if 1 mol% Al_2O_3 were mixed with pure $MgAl_2O_4$, the resulting solid solution would have 0.990 and 2.007 Mg and Al cations, respectively, per four oxygen ions. With 2% Al_2O_3, Mg would decrease to 0.980 and Al would increase to 2.013. These points, coded "theoretical" and labelled with the appropriate mole percent Al_2O_3, are shown for reference in Fig. 2. Comparison of these data points for $MgAl_2O_4$-Al_2O_3 solid solutions with the B6 data shows that the compositions of the B6 spinel are consistent with the presence of 1 to ~2.3 mol% excess Al_2O_3. Solid solution of Al_2O_3 in CAI spinel has been reported previously (EL GORESY et al., 1984) in an ultra-refractory rim sequence that includes hibonite and Sc-fassaite, and experiments by VIERTEL and SEIFERT (1980) have shown that, in the presence of corundum, the solubility of Al_2O_3 in $MgAl_2O_4$ increases with increasing temperature. Although the outermost spinel in B6, i.e., that which presumably formed first and at the highest temperature, is not significantly enriched in Al_2O_3 relative to spinel in the interior of B6, excess Al_2O_3 in the B6 spinel is consistent with the high-temperature history inferred for this inclusion (see Discussion).

Table 1. Representative electron probe analyses of spinel from Murchison spinel-hibonite spherules.

	<----------B6---------->			BB-1	H2-5
	1.	2.	3.	1.	2.
MgO	27.82	27.70	27.86	28.20	27.92
Al_2O_3	70.99	71.69	71.95	70.96	70.19
SiO_2	0.11	0.10	0.09	0.02	0.15
CaO	0.11	0.10	0.09	0.07	0.13
TiO_2	0.13	0.09	0.07	0.33	0.23
Cr_2O_3	0.12	0.11	0.13	0.12	0.07
V_2O_3	0.09	0.13	0.11	0.38	0.66
FeO	0.11	0.12	0.09	0.05	0.08
	99.48	100.04	100.39	100.13	99.43
Cations per 4 oxygen ions					
Mg	0.988	0.978	0.980	0.996	0.994
Al	1.994	2.002	2.002	1.983	1.977
Si	0.003	0.002	0.002	0	0.004
Ca	0.003	0.002	0.002	0.002	0.003
Ti	0.002	0.002	0.001	0.006	0.004
Cr	0.002	0.002	0.002	0.002	0.001
V	0.002	0.002	0.002	0.007	0.013
Fe	0.002	0.002	0.002	0.001	0.002
Total cations	2.996	2.992	2.993	2.997	2.998

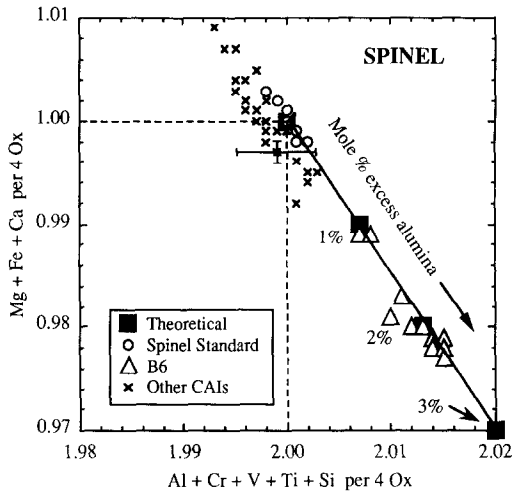

FIG. 2. Analyses of spinel showing an excess of Al-site cations and a deficit of Mg-site cations in B6 relative to stoichiometric $MgAl_2O_4$ (at intersection of lines) and to spinel in other CAIs. All analyses were collected on the same day under the same conditions and have been corrected as described in text. Representative 1σ error bars due to counting statistics are shown. Solid squares labelled "1%" and "2%" show the compositions of $MgAl_2O_4$-Al_2O_3 solid solutions with the indicated amounts of excess Al_2O_3, which are similar to the compositions of B6 spinel.

Hibonite

Electron microprobe analyses of hibonite from B6 are given in Table 2. Although endmember hibonite is $CaAl_{12}O_{19}$, most

Table 2. Representative analyses of hibonite from B6.

	1.	2.	3.
MgO	3.28	2.58	2.93
Al_2O_3	80.36	82.53	82.75
SiO_2	0.12	0.31	0.22
CaO	8.45	8.37	8.47
TiO_2	6.73	4.60	5.58
V_2O_3	0.14	0.12	0.11
FeO	0.02	0.02	0.02
	99.10	98.53	100.08
Cations per 19 oxygen ions			
Mg	0.558	0.439	0.492
Al	10.809	11.109	10.987
Si	0.014	0.035	0.025
Ca	1.033	1.024	1.022
Ti	0.578	0.395	0.473
V	0.006	0.006	0.005
Fe	0.001	0.002	0.002
Total cations	12.999	13.010	13.006

Sc_2O_3 was looked for but in all cases was below the detection limit of 0.031 wt % Sc_2O_3.

Table 3. Analyses of $CaAl_4O_7$ from B6.

	1.	2.	3.
MgO	0.03	0.03	0.03
Al_2O_3	77.76	77.60	77.25
SiO_2	0.10	0.09	0.07
CaO	21.90	22.04	21.98
TiO_2	0.17	0.19	0.17
V_2O_3	0.03	b.d.	b.d.
FeO	0.01	0.01	0.02
	100.00	99.96	99.52
Cations per 7 oxygen ions			
Mg	0.002	0.002	0.002
Al	3.972	3.968	3.968
Si	0.004	0.004	0.002
Ca	1.017	1.025	1.027
Ti	0.006	0.006	0.006
V	0.001	0	0
Fe	0	0	0
Total cations	5.002	5.005	5.005

b.d.: below detection limit. In all cases Sc_2O_3 was below the detection limit of 0.037 wt%.

meteoritic hibonite contains significant amounts of MgO and TiO_2, up to ~5 and 9 wt%, respectively (e.g., KEIL and FUCHS, 1971; MACPHERSON et al., 1983). These elements enter hibonite by the coupled substitution of $Mg^{2+} + Ti^{4+}$ for $2Al^{3+}$. The TiO_2 contents of one radially oriented hibonite lath adjacent to the large cavity near the center of Fig. 1a range from 6.7 wt% (analysis no. 1 in Table 2) to 4.6 wt% (analysis no. 2 in Table 2). The TiO_2-rich end of the lath is the one nearest the outer part of the inclusion and the TiO_2-poor end is the one nearest the core of the inclusion. The TiO_2 (and MgO) contents of the other hibonite crystals in B6 that are wide enough to analyze are within the ranges for these oxides found in the crystal described above. The average composition is approximately $CaAl_{11}Mg_{0.5}Ti_{0.5}O_{19}$. The V_2O_3 contents of the hibonite average 0.13 wt%. They are similar to those observed by MACPHERSON et al. (1983) and are within the range reported by IRELAND (1988) for hibonite from Murchison. One Murchison inclusion, however, described by ARMSTRONG et al. (1982), has hibonite with ~1 wt% V_2O_3.

$CaAl_4O_7$

Analyses of $CaAl_4O_7$ are given in Table 3. Like previously reported occurrences in other meteorites (e.g., MICHEL-LÉVY et al., 1982; BISCHOFF et al., 1993a), the $CaAl_4O_7$ in B6 is rather pure and uniform, with very low MgO, SiO_2, Sc_2O_3, TiO_2, V_2O_3, and FeO contents. Our analyses give slightly less than four Al cations, and slightly more than one Ca cation per seven oxygen ions, whereas most other analyses are closer to stoichiometric $CaAl_4O_7$ (e.g., BISCHOFF et al., 1993a,b). Although we have not made careful repeat analyses of Ca in our diopside standard comparable to those of Mg and Al in the spinel standard, the data for $CaAl_4O_7$, if taken at face value, would be consistent with ~0.5 mol% excess CaO.

Other Phases

Analyses of melilite and pyroxene from the rim of B6 are given in Table 4. The anorthite layer is too thin for a clean analysis. The melilite is aluminous ($Åk_{5-6}$), within the range ($Åk_{3-25}$) reported by MACPHERSON et al. (1983) for melilite in the rims of melilite-rich Murchison inclusions.

The pyroxene in the rim is zoned, with TiO_2 and Al_2O_3 contents decreasing from the anorthite-pyroxene contact outward. As illustrated by the analyses in Table 4, pyroxene compositions range from fassaite with ~15% Al_2O_3 and 3–

Table 4. Electron microprobe analyses of melilite and pyroxene in the rim of B6.

	Melilite		<-------Pyroxene------->		
	1.	2.	1.	2.	3.
MgO	0.79	0.95	11.42	16.05	19.03
Al_2O_3	35.24	34.89	15.27	5.97	2.27
SiO_2	22.95	23.07	44.88	50.58	53.06
CaO	40.76	40.91	24.90	25.77	25.15
Sc_2O_3	b.d.	b.d.	0.16	b.d.	b.d.
TiO_2	0.07	0.02	3.42	1.46	0.53
V_2O_3	b.d.	b.d.	0.14	0.17	0.20
FeO	b.d.	b.d.	0.08	0.05	0.08
	99.81	99.84	100.27	100.05	100.32
Mg	0.054	0.065	0.615	0.866	1.022
Al	1.898	1.880	0.650	0.255	0.096
Si	1.049	1.055	1.622	1.831	1.911
Ca	1.996	2.004	0.964	1.000	0.971
Sc	0	0	0.005	0	0
Ti	0.002	0.001	0.093	0.040	0.014
V	0	0	0.004	0.005	0.006
Fe	0	0	0.002	0.002	0.002
Total cations	4.999	5.005	3.955	3.999	4.022
No. of ox.	7	7	6	6	6
X_{Ak}	5.0	5.7	---	---	---

b.d.: below detection limit of 0.054 wt % Sc_2O_3, 0.023 wt % V_2O_3 and 0.030 wt % FeO in melilite; and 0.030 wt % Sc_2O_3 in pyroxene.

4 wt% TiO_2 (pyroxene analysis no. 1) through low-Al, low-Ti diopside (pyroxene analysis no. 2), to nearly pure diopside at the outermost part of the rim (pyroxene analysis no. 3). This pyroxene has less Al_2O_3 than the rim pyroxene described by MACPHERSON et al. (1983), and the latter has a wider range of TiO_2 contents (~0.5–7.5 wt%).

Only one of the perovskite grains in B6 is large enough for analysis. It has Ca and Ti in 1:1 atomic proportions, with ~0.2 wt% V_2O_3 and no detectable Y_2O_3. It may have ~0.8 wt% Al_2O_3, but we cannot completely rule out the possibility of contamination by adjacent spinel.

Bulk Chemical Composition

We analyzed a chip of B6 by INAA and several points by ion probe, and the results are given in Table 5. Contents of volatile elements (e.g., Na, Au) are very low and within the ranges of those observed in the relatively lightly altered inclusions found in Murchison (EKAMBARAM et al., 1984) and in the reduced subgroup of CV3 chondrites (BISCHOFF et al., 1987; SYLVESTER et al., 1992, 1993). This is consistent with the lack of alteration products in the thin section of B6 (Fig. 1a).

Table 5. Major, minor and trace element abundances in B6 (ppm unless otherwise indicated).

	INAA	IMP[1]	IMP[2]	IMP[3]	IMP[4]	IMP[5]
MgO (%)	14.7 ± 1.0	6.08	18.2	0.739	21.6	13.0
Al_2O_3 (%)	49.6	46.3	75.9	44.8	68.8	11.6
SiO_2 (%)	18.5[6]	2.81	0.908	10.1	1.80	49.4
CaO (%)	15.3 ± 0.9	26.7	2.51	27.1	4.62	24.8
TiO_2 (%)	1.86 ± 0.22	16.2	1.58	12.7	2.19	0.780
FeO (%)	0.628	1.25	0.496 ± 0.041	0.273 ± 0.071	0.176±0.021	0.218 ± 0.039
Na	357 ± 28	889	198	25330[7]	3409	85.0
K	150 ± 42	128	81.2	1675	127	33.2 ± 3.0
Sc	81.7	282	30.3 ± 2.2	267 ± 18	32.0 ± 2.4	164
V	428 ± 38	510	626 ± 79	149 ± 19	802 ± 113	343
Cr	585	773	1061	187 ± 28	1435	292 ± 17
Mn	105 ± 12	147 ± 11	112 ± 8	< 42	86.3 ± 8.7	< 32
Co	20.2	—	—	—	—	—
Ni	643	—	—	—	—	—
Zn	< 30	—	—	—	—	—
Ga	< 1.6	—	—	—	—	—
As	< 0.14	—	—	—	—	—
Se	0.71 ± 0.29	—	—	—	—	—
Br	0.298 ± 0.093	—	—	—	—	—
Sr	147 ± 41	216	56.5	186 ± 10	48.0	81.1
Y	—	37.4	0.38 ± 0.16	31.0 ± 3.7	4.93 ± 0.55	1.76 ± 0.34
Zr	< 53	108	3.68 ± 0.82	119 ± 12	19.4 ± 1.9	7.3 ± 1.2
Nb	—	87.1	0.93 ± 0.38	68.5 ± 8.6	11.2 ± 1.3	0.63 ± 0.31
Mo	1.03 ± 0.44	—	—	—	—	—
Ru	0.80 ± 0.23	—	—	—	—	—
Sb	< 0.18	—	—	—	—	—
Cs	0.189 ± 0.057	< 0.71	< 0.66	< 4.6	< 0.64	< 0.67
Ba	< 45	16.5 ± 1.8	31.5 ± 2.3	54.7 ± 8.1	6.1 ± 1.0	10.0 ± 1.3
La	7.64	96.0	3.08 ± 0.30	91.3	24.9	1.47 ± 0.20
Ce	21.4	301	7.46 ± 0.74	349	80.1	5.27 ± 0.62
Pr	—	47.4 ± 2.5	0.90 ± 0.34	66.1 ± 7.7	12.6 ± 1.2	0.51 ± 0.25
Nd	—	236	4.1 ± 1.2	267 ± 25	53.9 ± 4.2	4.2 ± 1.2
Sm	5.57	78.4	1.06 ± 0.27	117 ± 7	22.8 ± 1.2	1.41 ± 0.30
Eu	0.584 ± 0.039	2.13 ± 0.34	0.47 ± 0.12	3.5 ± 1.1	0.81 ± 0.18	0.42 ± 0.11
Gd	—	12.7 ± 4.2	< 0.89	50.3 ± 18.3	< 5.4	1.29 ± 0.58
Tb	0.573	3.72 ± 0.78	< 0.15	15.4 ± 3.5	< 0.92	< 0.23
Dy	3.72 ± 0.19	29.8 ± 2.4	< 0.41	108 ± 11	6.8 ± 1.4	1.07 ± 0.41
Ho	0.331 ± 0.052	1.07 ± 0.46	< 0.16	5.0 ± 2.4	< 0.59	< 0.32
Er	—	2.89 ± 0.98	< 0.30	17.3 ± 4.9	<1.2	0.57 ± 0.24
Tm	0.561 ± 0.048	4.22 ± 0.34	< 0.094	18.5 ± 2.1	1.58 ± 0.23	< 0.13
Yb	2.26	15.6	< 0.35	35.0 ± 7.7	4.94 ± 1.00	2.49 ± 0.58
Lu	0.0508±0.0090	1.19 ± 0.44	< 0.11	< 4.1	<0.50	< 0.18
Hf	< 0.14	—	—	—	—	—
Ta	0.285 ± 0.042	—	—	—	—	—
W	< 0.19	—	—	—	—	—
Re	0.037 ± 0.011	—	—	—	—	—
Os	0.50 ± 0.12	—	—	—	—	—
Ir	0.507	—	—	—	—	—
Au	0.0032 ± 0.0014	—	—	—	—	—
Th	0.784 ± 0.044	3.26 ± 0.43	< 0.25	1.48 ± 0.86	1.18 ± 0.29	< 0.14
U	< 0.14	0.87 ± 0.22	< 0.14	1.46 ± 0.84	<0.24	< 0.14

Errors are ±1σ based on counting statistics, and are only given where they exceed 5% of the amount present; upper limits are <2σ. [1]Perovskite-rich ion microprobe (IMP) spot also including spinel and hibonite. [2]Spinel-hibonite spot. [3]$CaAl_4O_7$ - perovskite spot. [4]Spinel-hibonite-perovskite spot. [5]Pyroxene-anorthite spot in rim. [6]Determined by difference. [7]High Na probably due to penetration of ion beam into epoxy mounting medium.

Chondrite-normalized rare earth element (REE) abundances are plotted in Fig. 3. The bulk pattern can be classified as Group II, characterized as having relatively high, flat light REE abundances, progressively decreasing heavy REE (HREE) abundances from Gd through Lu, negative Eu and Yb anomalies and positive Tm anomalies. Group II patterns are not unusual for oxide-rich refractory inclusions. EKAMBARAM et al. (1984) analyzed several spinel-hibonite spherules from Murchison and found two with Group II patterns. Ion microprobe studies have shown that Group II patterns are common among hibonite-bearing inclusions from C2 chondrites (FAHEY et al., 1987; HINTON et al., 1988; IRELAND et al., 1988; IRELAND, 1990). BISCHOFF et al. (1992) analyzed Ca-dialuminate-bearing refractory inclusions from two CR-type meteorites and one unique chondrite (Acfer 182) and found that they too have Group II patterns, and KIMURA et al. (1993) reported modified Group II patterns in three of four $CaAl_4O_7$-bearing inclusions which they analyzed from ALH85085.

Abundances of refractory siderophile elements (Mo, Ru, Re, and Os) in B6 are within error of those in C1 chondrites; Ir, which has the smallest uncertainty, has an enrichment factor of $1.06 \pm 0.01 \times$ C1. This is somewhat unusual for a Group II inclusion, because this type of inclusion typically has subchondritic abundances of refractory siderophiles (e.g., CONARD, 1976; GROSSMAN and GANAPATHY, 1976).

Chemical and Isotopic Composition of Individual Spots

The ion probe data show that perovskite is the major REE carrier among the oxide phases. Compare, for example, the ion probe analysis of a perovskite-rich spot (Table 5, column 2) with one of a perovskite-free spot (Table 5, column 3). The Group II pattern of the bulk inclusion is evident from the ion microprobe analyses of the primary phases. Yttrium has an ionic radius intermediate between those of Dy and Ho, so mineral-mineral and mineral-melt fractionation generally gives Y enrichment factors intermediate between those of Dy and Ho. Yttrium is more refractory than Dy and Ho and about as refractory as Lu, so Group II inclusions, including B6, generally show an Y depletion relative to Dy and Ho. The REE pattern of the silicate rim is quite distinct from that of the interior. In comparing, for example, the perovskite-, hibonite-, spinel-containing spot (Table 5, column 2) in the interior with the pyroxene-, anorthite-containing spot (Table 5, column 6) in the rim, it is seen that enrichment factors for most REEs in the rim are a factor of ~40 lower than in the interior, except for Eu and Yb, the two most volatile REEs, which are lower in the rim by only a factor of 5. This observation is in direct contrast to that of BOYNTON and WARK (1987) who found that similar rims on CAIs in C3 chondrites are invariably enriched in all REEs except Eu and Yb relative to their respective interiors.

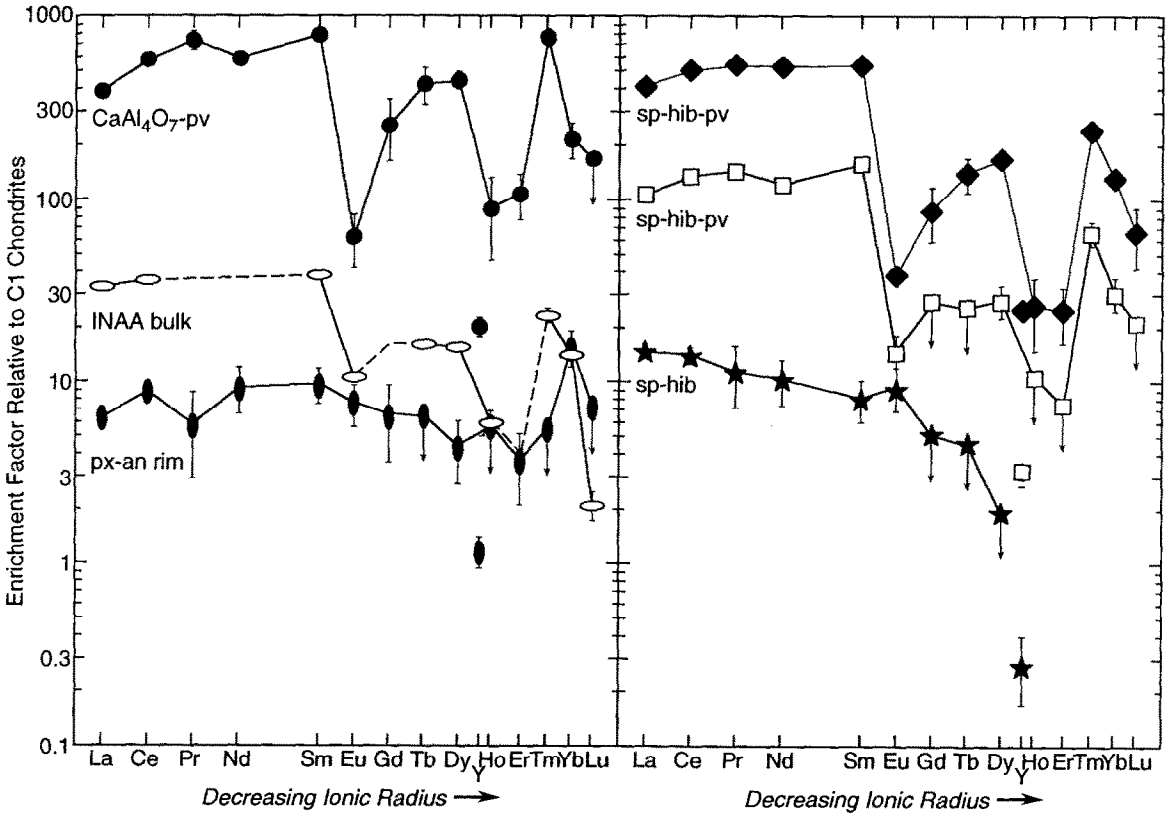

FIG. 3. Chondrite-normalized rare-earth element and Y abundances in B6, determined by INAA (open ovals) and by ion probe.

Magnesium isotopic data for B6 are shown in Table 6. Three spots in interior phases show no isotopic mass fractionation effects; combined together they give $\Delta^{25}Mg = 0.0 \pm 2.5‰$ ($\pm 2\sigma$). In contrast the melilite-anorthite-pyroxene rim is enriched in the heavy isotopes of Mg by about 10‰/amu. The only phase with a high Al/Mg ratio, $CaAl_4O_7$, has substantial excess ^{26}Mg. An isochron through data collected in the interior of B6 has a slope corresponding to an $^{26}Al/^{27}Al$ ratio of $(2.91 \pm 0.78) \times 10^{-5}$ at the time of isotopic closure. This ratio is slightly lower than the canonical early solar system $^{26}Al/^{27}Al$ ratio of $\sim 4.5 \times 10^{-5}$ (MACPHERSON et al., 1992). The ^{26}Al-^{26}Mg systematics of B6 are consistent with previous studies of hibonite-rich inclusions from Murchison: spinel-hibonite inclusions quite commonly have excess ^{26}Mg consistent with a $^{26}Al/^{27}Al$ ratio of $\sim 4.5 \times 10^{-5}$, while monomineralic hibonite crystal fragments generally do not show excess ^{26}Mg despite having high $^{27}Al/^{24}Mg$ ratios (IRELAND, 1990).

DISCUSSION

Crystallization History

From its spherical shape and the radial orientation of many of the hibonite laths, we can infer a liquid origin for the oxide phases in B6. Note the small spray of hibonite laths, visible in Fig. 1a, which apparently nucleated at what is now the spinel-melilite contact and grew inward, diverging from their nucleation point as they did. A spray of crystals like this is especially strong evidence that B6 was a molten droplet that cooled by radiating heat from its surface. As argued by MACPHERSON et al. (1983), condensation from a vapor would not give rise to crystal sprays on the edges of inclusions, because in that case there would be no surface for the crystals to preferentially nucleate upon. In addition, phase equilibria (discussed below) show that spinel + hibonite is a higher temperature assemblage than that found in the core, further evidence that B6 formed by inward crystallization of a molten droplet. It is unlikely that spinel crystallized in the interior of the inclusion, migrated to the rim, and remained there due to surface tension effects. MACPHERSON et al. (1983) described spherules of similar chemical and mineralogical composition to B6 which contain spinel crystals throughout their interiors. This shows that if spinel nucleates everywhere in the inclusion, it does not necessarily migrate to the outside.

BOYNTON and WARK (1987) concluded that the rims on the CAIs they studied are evaporation residues of the interiors. Evaporation of the interior cannot explain the REE pattern of the rim of B6, however. Rather, it probably formed by deposition of condensates from a reservoir which had become enriched in Eu and Yb relative to the other REEs. Because the abundances of the major elements determined by INAA in the bulk sample are strongly affected by contributions from the silicates in the rim, they do not truly reflect the composition of the original spherule. We therefore calculated the silicate-free bulk composition of the interior of the inclusion, as described below.

Because the larger of the two splits of B6 was used for INAA and because of the low probability that the random plane exposed in the thin section of the other split of B6 samples representatively the true proportions of core (calcium dialuminate + perovskite) to mantle (hibonite + spinel) to rim (clinopyroxene + anorthite + melilite) in this concentrically zoned inclusion, the mineral proportions used below are derived from the INAA data in Table 5, rather than from a point-count of the thin section. Using the electron microprobe analyses of all phases in B6 except perovskite and anorthite, for which stoichiometric compositions were used, a mineralogical composition was calculated from the INAA data and their uncertainties which reproduces the mineral proportions within each of the zones, specifically weight ratios of calcium dialuminate/perovskite and spinel/hibonite of 7.1 and 3.8, respectively, determined by point-counting 1215 grid points on the SEM photo of the thin section. The calculated mineral proportions, in weight percent, of the whole inclusion are spinel, 36.5; calcium dialuminate, 10.3; hibonite, 9.73; perovskite, 1.44; clinopyroxene, 27.5; anorthite, 7.06; and melilite, 7.78. These translate into the following volume percentages: core, 12.7; mantle, 42.3; and rim, 45.0. These proportions are significantly different from those obtained by converting the thicknesses of the zones as measured on the SEM photo to volume percent: core, 9.60; mantle, 43.0; and rim, 47.4. This discrepancy can be reconciled quantitatively if the plane of the thin section is 20 μm from the equatorial plane of the entire inclusion, a reasonable displacement considering that the radius of the inclusion in thin section is 83 μm. The amounts of oxides contributed by the rim phases, clinopyroxene, anorthite, and melilite, were subtracted from the INAA data which were then renormalized, yielding 73.2 wt% Al_2O_3, 17.7% MgO, 6.5% CaO, and 2.5% TiO_2, for the core and mantle of B6.

The bulk composition of B6 is very similar to that of BB-2, a hibonite-spinel spherule described by MACPHERSON et al. (1983). We normalized the bulk compositions of both inclusions to 100% Al_2O_3 + MgO + CaO and plotted them on the MgO – Al_2O_3 – CaO ternary phase diagram (Fig. 4) in order to interpret their crystallization sequences. Due to the high temperatures involved, experimental data for the extremely Al_2O_3-rich part of this system are scarce. We therefore used phase relations that were calculated from thermodynamic data (BERMAN, 1983). Temperatures are probably accurate to within ~20–30°C (J. Beckett, pers. commun.). Both B6 and BB-2 plot well into the spinel stability field and have calculated liquidus temperatures of about 2110°C. As liquids with these compositions crystallize spinel, the residual liquid compositions move directly away from spinel toward the spinel-hibonite cotectic, as shown by the

Table 6. Magnesium isotopic compositions in B6.

Spot	$^{27}Al/^{24}Mg$	$\Delta^{25}Mg$(‰)	$\delta^{26}Mg$(‰)
sp-hib	5.8 ± 1.7	-1.3 ± 3.6	1.1 ± 4.8
sp-hib	2.92 ± 0.09	-1.4 ± 5.6	-0.6 ± 7.6
sp-hib	8.77 ± 0.32	2.7 ± 3.3	4.5 ± 4.3
$CaAl_4O_7$	247 ± 22	7.8 ± 7.3	49 ± 13
ge-sp-an	10.41 ± 0.66	10.6 ± 5.0	2.8 ± 6.0
sil rim	0.166 ± 0.005	7.1 ± 4.4	-3.9 ± 5.7
sil rim	0.154 ± 0.004	10.7 ± 3.7	2.8 ± 3.0

Uncertainties are $\pm 2\sigma$.

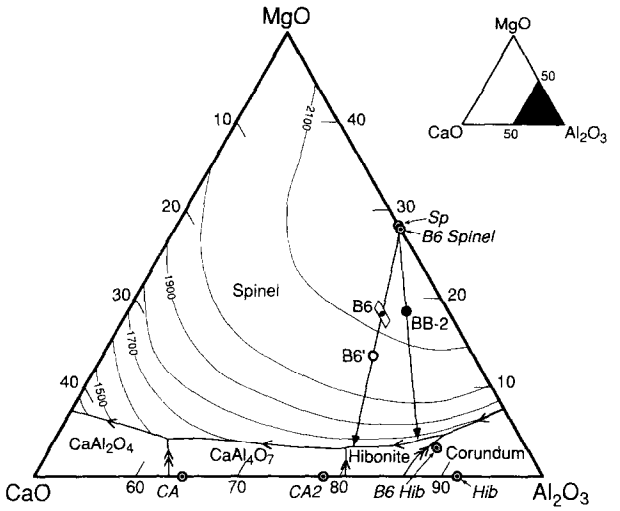

FIG. 4. Calculated liquidus phase relations in the Al-rich portion of the Al_2O_3–MgO–CaO system. The parallelogram around the bulk composition of B6 reflects the 1σ errors in the INAA data. Arrows through B6 and BB-2 bulk compositions show paths of residual liquid compositions during spinel crystallization. The average composition of B6 spinel was used to model B6 fractionation, and stoichiometric $MgAl_2O_4$ was used for BB-2. Open circle labelled B6′ represents the composition of the B6 liquid after crystallization of 32 wt% spinel. Abbreviations as used previously, except: CA: $CaAl_2O_4$; CA2: $CaAl_4O_7$. Compositions are in wt% oxide; temperatures are in °C. After BERMAN (1983).

arrows through the data points in Fig. 4. For B6, this cotectic would be reached at ~1730°C, with hibonite and spinel co-crystallizing until the spinel-hibonite-$CaAl_4O_7$ invariant point is reached, at ~1725°C. At this point, the $CaAl_4O_7$ begins to crystallize, and spinel and hibonite continue to do so. This is the same crystallization sequence we infer for B6 based on its texture, assuming inward crystallization from what is now the spinel-melilite contact. The outer shell of nearly pure spinel indicates that spinel crystallized first. The shell had almost completely enclosed the inclusion when hibonite began crystallizing. Hibonite and spinel then co-crystallized, forming the spinel + hibonite zone. This was followed by formation of the $CaAl_4O_7$-rich core, which contains perovskite due to the presence of TiO_2. Some hibonite laths extend into the $CaAl_4O_7$, indicating that the last hibonite co-crystallized with $CaAl_4O_7$. The same spinel grains that were crystallizing with hibonite in the mantle presumably continued to grow after $CaAl_4O_7$ precipitated, accounting for the absence of spinel enclosed by $CaAl_4O_7$ in the core.

BB-2, on the other hand, does not have a spinel-rich mantle like B6 does. In BB-2, many hibonite laths nucleated at or near the outer edge of the inclusion (MACPHERSON et al., 1983), although, like B6, its composition plots in the spinel field (Fig. 4). Thus, as pointed out by MACPHERSON et al. (1983), this sample may not have been completely molten. By assuming that the hibonite in BB-2 was completely molten but the spinel was not, MACPHERSON et al. (1983) estimated temperatures of 1780°C for the onset of hibonite crystallization in the pure ternary system, and 1550°C when taking into account the lowering of its melting point due to its non-zero TiO_2 and MgO contents. Also, despite the fact that its composition is quite similar to that of B6 and thus has the same equilibrium crystallization sequence, BB-2 does not contain $CaAl_4O_7$, and appears to have crystallized hibonite + spinel first, followed by hibonite + spinel + perovskite. This contrasts with the sequence that is consistent with the phase equilibria and with the petrography of B6. BB-2 may have cooled more quickly than B6, so that hibonite and spinel continued to crystallize metastably instead of being joined by $CaAl_4O_7$. Additionally, the slightly higher TiO_2 content of BB-2 relative to that of B6 (~3 vs. ~2.5 wt%) may have expanded the hibonite stability field relative to that of $CaAl_4O_7$, so that $CaAl_4O_7$ could not crystallize. Although not experimentally reproduced at that time, this effect was suggested by MACPHERSON et al. (1983) as an explanation for the absence of $CaAl_4O_7$ from BB-2.

Recently, BECKETT and STOLPER (1994) investigated a TiO_2-free liquid composition from which spinel and $CaAl_4O_7$ crystallized. When they added just 1 wt% TiO_2 to that bulk composition, spinel + hibonite, rather than spinel + $CaAl_4O_7$, crystallized from it. This led BECKETT and STOLPER (1994) to conclude that, with increasing Ti in the liquid, the activity of $CaAl_4O_7$ decreases, decreasing the size of its stability field relative to that of hibonite. This effect may not only account for the absence of $CaAl_4O_7$ from BB-2, but also for the rarity of $CaAl_4O_7$ in hibonite-bearing inclusions in general, because most of these inclusions contain several weight percent TiO_2. The paucity of corundum-bearing inclusions might also be understood in this light, because corundum formation requires not only high Al_2O_3 abundances, but also very low MgO, TiO_2, and CaO abundances. Corundum is predicted to be the first major phase to condense from a gas of solar composition (GROSSMAN, 1972), but very little of it was removed from the gas and preserved in meteorites. Instead, almost all condensate corundum apparently either continued to react with the nebular gas or entered hibonite-, perovskite-rich assemblages, which, when melted, gave rise to liquids that contained sufficient amounts of oxides other than Al_2O_3 that corundum could not crystallize.

Maximum Temperature Reached by B6

Evidence from phase relations

The presence of a nearly pure spinel shell, visible in Fig. 1a, outside of the hibonite + spinel zone in B6 indicates that, during the crystallization of this inclusion, there was a significant interval during which only spinel crystallized, consistent with the phase equilibria (Fig. 4). This also indicates that B6 was initially either completely molten, or very nearly so. If B6 were completely molten, its liquidus temperature inferred from phase relations in the Al_2O_3–CaO–MgO system (BERMAN, 1983) would be about 2110 ± 30°C. This is the maximum crystallization temperature we can infer for B6. The small amount of TiO_2 present would probably not strongly affect the stability of spinel, or the phase relations in general (with the exception of expansion of the hibonite field at the expense of the $CaAl_4O_7$ field), as compared to the TiO_2-free system (BECKETT and STOLPER, 1994).

If B6 were not completely molten, it could have experienced a lower peak temperature than that given above. From the texture and the phase relations, we can assume that the perovskite, $CaAl_4O_7$, hibonite, and the fraction of spinel that is in the pure spinel shell were molten. Let us now further assume that the remaining spinel is relict. From the thickness of the spinel shell seen in the photomicrograph (Fig. 1a), corrected for off-center sectioning as described earlier, we estimate that the spinel shell accounts for 26 vol% (or 27 wt%) of the inclusion. If we assume that all the spinel in the shell crystallized before hibonite, this would represent the minimum amount of spinel that crystallized before the spinel-hibonite cotectic was reached. Application of the lever rule to the phase diagram (Fig. 4) shows that 59 wt% of a liquid having the composition of B6 will crystallize as spinel prior to the appearance of hibonite. If only 27 wt% spinel crystallized from the melt, then 32 wt% is relict. In this case, the corresponding liquid composition would have 32 wt% less spinel than the B6 bulk composition. This liquid, represented on Fig. 4 by the open circle labelled B6′, has a calculated liquidus temperature of ~2080°C, ~30° lower than if B6 were completely molten. Within the TiO_2-free system, this is the minimum estimate of the initial crystallization temperature of B6, because it is based on the minimum amount of spinel that could have crystallized prior to hibonite; crystallization of higher amounts of pre-hibonite spinel would move the B6′ composition up-temperature in Fig. 4, toward spinel and the B6 bulk composition. Even so, this temperature is ~530°C higher than the minimum inferred for BB-2 (MACPHERSON et al., 1983), making it the highest temperature indicated for any refractory inclusion.

Evidence from spinel compositions

Analysis of experimentally produced corundum-, spinel-bearing assemblages shows that significant solid solubility of Al_2O_3 in $MgAl_2O_4$ is possible, and that the solubility increases with increasing temperature. VIERTEL and SEIFERT (1980) found 10 mol% excess Al_2O_3 (relative to stoichiometric $MgAl_2O_4$) in spinel crystallized at 1300°C, and SIMON et al. (1993b) found 24 mol% in spinel formed at 1450°C. Although Type B CAIs crystallized at temperatures within this range (STOLPER and PAQUE, 1986), they do not contain corundum and the spinel grains in them, unlike those in the experimental runs, do not have detectable excess Al_2O_3. This is because the presence or absence of corundum and amount of excess Al_2O_3 in spinel depend not only upon temperature but also on the ratio of the activity of Al_2O_3 ($a_{Al_2O_3}$) to that of MgO (a_{MgO}) in the system. Experiments with solids by CHAMBERLIN et al. (1992) show that excess Al_2O_3 in spinel is positively correlated with $a_{Al_2O_3}/a_{MgO}$, and we can infer that solubility of Al_2O_3 in spinel should be positively correlated with $a_{Al_2O_3}/a_{MgO}$ of coexisting liquids, and with temperature at constant $a_{Al_2O_3}/a_{MgO}$. Using the method of BERMAN (1983), SIMON et al. (1993b) determined that the experimental run products they analyzed all have $a_{Al_2O_3}/a_{MgO} > 6$, whereas in Type B inclusions, liquids with which spinel equilibrated, had $a_{Al_2O_3}/a_{MgO} \sim 1$. They concluded that spinel in CAIs has negligible excess Al_2O_3 despite having crystallized at temperatures similar to those of the experimental run products, because the $a_{Al_2O_3}/a_{MgO}$ ratio is so much lower in CAIs than in their experimental runs. The B6 melt would also have $a_{Al_2O_3}/a_{MgO} \sim 1$ (BERMAN, 1983), but the spinel in this sample has 1–2 mol% excess Al_2O_3. This indicates that the equilibration temperature of B6 was substantially higher than that of Type B inclusions, which contain stoichiometric spinel. This is consistent with the texture and phase relations of B6, discussed above.

Implications of High Melting Temperatures

Figure 5 shows the extent to which B6 would have been out of equilibrium had it been melted in the presence of a gas of solar composition. For illustrative purposes, hibonite, a typical, very high-temperature, Al_2O_3-rich condensate, is used as a proxy for the entire mineral assemblage of B6. In the figure, the calculated variation of the condensation temperature of hibonite with pressure is extrapolated to the range of total pressure where its condensation temperature exceeds its incongruent melting temperature. In this region of the diagram, the slopes of both the gas-liquid and the liquid-solid phase boundaries are only schematic. The temperature interval for crystallization of B6 from a liquid is superimposed on the diagram. Even if melting of B6 occurred at 10^{-3} atm, the maximum pressure thought possible for all but a small part of the solar nebula, B6 would have been molten entirely within the stability field of vapor, from 250 to 600 K above the maximum temperature for stability of any condensed phase at this pressure and from 3 to 6 orders of magnitude below the minimum solar nebular pressure necessary for stabilizing liquids of these compositions. B6 would have been so far out of equilibrium that it should have been volatilizing rapidly.

Evaporative loss from a liquid is known to produce bulk residues enriched in the heavy isotopes of Mg, whereas evaporative loss from a solid produces magnesium isotopic fractionation effects in only the outer few micrometers with no significant effect on the bulk magnesium isotopic composition (DAVIS et al., 1990; WANG et al., 1991, 1993). As Table 6 shows, the interior phases of B6 show no measurable magnesium isotopic fractionation, with an average $\Delta^{25}Mg$ of 0 $\pm$ 2.5‰ (2σ). The only measured gas-liquid magnesium isotopic fractionation factors are the data of DAVIS et al. (1990) who found that they are invariant for forsterite composition over the temperature range 1900 to 2050°C. When isotopic fractionation is controlled by the kinetic isotope effect, the fractionation factor depends on the mass of the evaporating species. Because Mg evaporates as the monatomic species from solid and liquid forsterite, solid and liquid spinel, and from silicate liquids, we assume that the average magnesium isotopic fractionation factor found by DAVIS et al. (1990) is applicable to a liquid of B6 composition. Using the upper limit on $\Delta^{25}Mg$ of 2.5‰, we conclude that no more than 15% of the Mg could have evaporated from B6.

Vacuum evaporation rates for Mg have been measured as a function of temperature for liquid Mg_2SiO_4 by HASHIMOTO (1990), who found that they are kinetically hindered. Using

these rates, we calculated that the times required to evaporate 15% of the Mg from a melt droplet of the size and composition of B6 are 0.27, 0.88, 3.3, and 14 s at 2100, 2000, 1900, and 1800°C, respectively. If, instead, Mg evaporates from a melt of B6 composition at the theoretical rates predicted by thermodynamic equilibrium, the times for evaporation of 15% of the Mg are 0.078, 0.23, 0.72, and 2.6 s at 2100, 2000, 1900, and 1800°C, respectively. It is clear that if B6 were melted in a gas of normal solar nebular pressure, it must have spent very little time at these temperatures. B6 must not have been heated significantly above its liquidus temperature; detectable Mg loss would have occurred in under 0.1 s at 2200°C, for example.

In order to calculate a cooling curve for B6, we integrated the equation of MACPHERSON et al. (1984b) which relates the radiative cooling rate of a liquid spherule to the difference in temperature between the liquid and the surrounding gas. For this calculation, we used 70 μm for the radius of the silicate-free portion of B6 and assumed that the emissivity was 0.8; the density was 3.2 g cm^{-3}; the heat of crystallization was that of Al_2O_3, 1090 J g^{-1} (BERMAN and BROWN, 1984); and that the heat capacity of the B6 melt was 1.4 J g^{-1}K^{-1}, as calculated from a weighted average of the heat capacities of the oxide components which, as in RICHET and BOTTINGA (1980), were assumed to be 29.2 J afu^{-1}K^{-1}, where afu is the number of atoms per formula unit. Starting from its liquidus temperature of 2110°C (Fig. 5), B6 would have cooled to its solidus, 1725°C, in 0.25 s and would have thermally equilibrated with a surrounding gas at 1800 K in 0.6 s, after which it would have cooled at the same rate as the gas.

Evaporation of Mg from liquids at high temperatures is extremely rapid. Would more than 15% of the Mg have evaporated if B6 had cooled radiatively in a gas at 1800 K? We calculated the fraction of Mg evaporated at each temperature

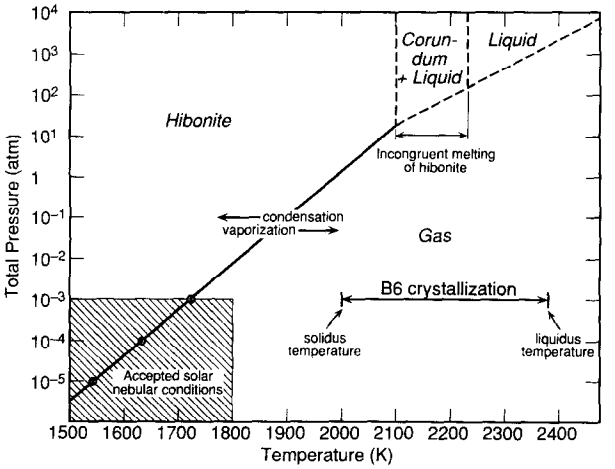

FIG. 5. Schematic phase diagram, with hibonite serving as a proxy for B6, showing how far out of equilibrium with a gas of solar composition B6 was while it was molten. At a maximum solar nebular pressure of 10^{-3} atm, the crystallization interval for B6 lies entirely within the field of gas, 250–600 K above the maximum temperature of stability of any major solid phase and 3 to 6 orders of magnitude below the minimum pressure required for the stabilization of liquids of this composition in a solar gas.

along the cooling curve calculated above. If Mg evaporated from the liquid at the measured rate for liquid Mg_2SiO_4 from the liquidus to the solidus temperature, 13% of the Mg would have evaporated by the time the solidus was reached; if Mg evaporated from the liquid at the theoretical rate from the liquidus to the solidus, 52% of the Mg would have evaporated by the time the solidus was reached. It is unlikely that such large fractions of the total Mg evaporated during radiative cooling of B6. The spinel shell probably began to form shortly after the peak temperature was reached, effectively sealing off the molten interior of the inclusion from the surrounding nebular gas. Evaporation of solid spinel could have occurred, but would not have fractionated magnesium isotopes in the interior of B6 significantly, because diffusion rates in solid spinel are too low to permit isotopic equilibration during evaporation (WANG et al., 1991, 1993).

Diffusion rates in liquid play an important role in crystallization. In order for the phases in B6 to have crystallized in concentric zones in the order predicted from the phase diagram, diffusion rates in the liquid must have been fast enough to permit Mg and Al atoms to diffuse to the edge of the inclusion and crystallize spinel. There are no experimental measurements of diffusion rates in liquids of B6 composition. The composition that has been studied that is closest to that of B6 is discussed by SHENG et al. (1992), who measured Mg diffusion rates in spinel and a coexisting melt similar in composition to plagioclase-olivine inclusions (45% SiO_2, 31% Al_2O_3, 13% MgO, and 11% CaO). Their highest temperature measurement is at 1553°C, so the data must be extrapolated by 175 to 540°C to cover the crystallization range of B6. We calculated characteristic diffusion times, $\tau = L^2/D$, where L is the length scale and D is the diffusion coefficient. Characteristic diffusion times at 2100, 2000, 1900, and 1800°C are 0.30, 0.64, 1.4, and 3.5 s for a distance equal to the radius of B6. If the Mg diffusion rate determined by SHENG et al. (1992) is applicable to B6, this calculation suggests that growth of the concentric structure would have been hindered in the radiative cooling time computed above. On the other hand, it is quite likely that Mg diffusion in the silica-free, B6 liquid composition is at least a factor of ten faster than in the siliceous melt studied by SHENG et al. (1992), and the large temperature extrapolation that we have made from measured diffusion rates may be inaccurate. In summary, diffusion rates may be important in determining the texture of B6, but the literature data on them are not sufficient to set strict time constraints on the growth of B6.

Because the temperatures required for the melting of spinel-rich spherules are in excess of 1725°C, and because models of the formation and evolution of the solar nebula suggest that such temperatures would be reached only near the center of the nebula, if anywhere, both MACDOUGALL (1981) and MACPHERSON et al. (1983) suggested hypervelocity impacts as a possible mechanism for generating the high temperatures required for the melting of solid precursors of oxide-rich Murchison spherules. These authors further suggested that such events would be more likely to yield the desired high temperatures if the condensates themselves were still hot when the impact occurred (MACDOUGALL, 1981), which, in turn, would be most likely if the surrounding nebular gas were hot

(MACPHERSON et al., 1983). Both of these suggestions also apply to B6.

The rapid cooling indicated by the undetectable fractionation of the magnesium isotopes in the interior of B6 places an important constraint on the mechanism of heating. Large-scale processes, such as shock waves, seem improbable because it is likely that they would heat large volumes of gas, which presumably would not cool rapidly. A small, isolated event, such as a hypervelocity impact which would virtually heat only the CAI itself, is required.

Formation of B6

In his study of twelve perovskite-spinel and hibonite-spinel spherules, MACDOUGALL (1981) proposed a sequence of events for their formation including condensation of oxide phases, melting of these precursors, crystallization of the melt, and then formation of silicate rims on the spherules. We propose a similar, somewhat more detailed sequence for the formation of B6, which is consistent with its petrography, phase relations, and chemistry.

Removal of ultrarefractory REE component from gas at ~1450°C

B6 has a Group II REE pattern, which is best modeled by removal of refractory REEs from a solar gas by an early condensate, followed by formation of the sample from that fractionated gas (BOYNTON, 1975; DAVIS and GROSSMAN, 1979). According to our models of condensation from a gas of solar composition, the first condensate phase that can remove significant amounts of REEs from the gas is hibonite, which condenses at ~1450°C at a total pressure of 10^{-3} atm (GEIGER et al., 1988). Perovskite is also a potential REE carrier, but its condensation temperature is ~50°C lower than that of hibonite.

Condensation of solid precursors

The record of prior REE removal from the gas was preserved in phases that condensed from the fractionated gas at temperatures <1450°C. Arguments against both equilibrium and metastable condensation of Al_2O_3-rich, SiO_2-poor liquids from the solar nebula are given by BAR-MATTHEWS et al. (1982). They pointed out that equilibrium condensation of such liquids would require temperatures and pressures much higher than those thought to have existed in the solar nebula, as can also be seen in Fig. 5. Metastable (subliquidus) condensation of a liquid would most likely have led to metastable crystallization, which is not consistent with the petrographic evidence for crystallization of phases in the same sequence as that predicted by phase equilibria. It is therefore most likely that the condensate precursors were solid.

Melting of solid precursors

The strong evidence against condensation of a liquid and for crystallization of the oxide phases in B6 from a liquid requires that B6 had solid precursors which were melted. This melting must have occurred before silicates began to condense (at ~1350°C with $p^{tot} = 10^{-3}$ atm). From the phase equilibria we estimate that B6 should have begun crystallizing spinel at a temperature of at least ~2080°C. This is much higher than current estimates of maximum temperatures in the solar nebula, except near its center. Heating in a local, transient event, such as a hypervelocity impact between early formed refractory condensates, seems to be the most plausible way to generate such a high temperature, as has been suggested previously (MACDOUGALL, 1981; BAR-MATTHEWS et al., 1982; MACPHERSON et al., 1983). From the excess ^{26}Mg in the $CaAl_4O_7$, which is evidence for in situ decay of ^{26}Al ($T_{1/2} = \sim 7.2 \times 10^5$ y), melting must have taken place fairly soon after condensation of the precursors.

Crystallization of oxide phases from the melt

Inward crystallization of a melt droplet is indicated by the texture (spherical shape; spinel layer; radially oriented hibonite laths including a diverging-inward spray; and a higher-temperature assemblage on the outside of a lower-temperature assemblage) and the phase equilibria. Spinel crystallized first, followed by spinel + hibonite, followed by $CaAl_4O_7$ + hibonite + spinel + perovskite. This is the predicted fractional crystallization sequence for a liquid with the silicate-free bulk composition of B6. Crystallization of the spinel shell very soon after melt formation is indicated by the unfractionated magnesium isotopes in B6, which require that little or no evaporation from the melt took place. Some evaporation of solid spinel could have occurred, possibly corroding the outer boundary of the spinel layer.

Deposition of silicate layers

The oxide assemblage in B6 is enclosed by concentric layers, from inside to out, of melilite, anorthite, and clinopyroxene, the same sequence observed by MACPHERSON et al. (1983) on the outside of a melilite-rich inclusion from Murchison, MUM-1. Those workers favored formation of the rims by metasomatic reaction of the melilite during which significant amounts of material, particularly MgO and SiO_2, were introduced into the rim layers from the nebular gas, as proposed for Allende inclusions by MACPHERSON et al. (1981). The compositions of the interiors are so different from one another, however, with B6 containing much less SiO_2 and CaO than MUM-1, that formation of identical sequences of rim layers by reaction of the nebular gas with the interiors of both inclusions seems highly unlikely. The silicate rim layers on B6 probably formed by deposition of fresh condensates around the silica-free core. Further evidence for the absence of a significant contribution of material from the core of B6 to the rim layers comes from the sharply contrasting REE patterns and distinctly different magnesium isotopic compositions of core and rim, although the isotopic difference could possibly reflect evaporative loss of Mg after rim deposition.

CONCLUSIONS

We have described herein a spinel-, hibonite-, $CaAl_4O_7$-, perovskite-bearing spherule and have presented strong evi-

dence that it crystallized from a liquid. The phase equilibria indicate that a very high temperature, at least 2080°C, was reached, the highest temperature yet inferred for a refractory inclusion. The presence of measurable excess Al_2O_3 in B6 spinel despite the normal $a_{Al_2O_3}/a_{MgO}$ ratio of the inclusion is further evidence of its unusually high temperature history. Despite the high peak temperature, no volatility-derived fractionation of REEs or isotopic fractionation of Mg occurred, probably because cooling was very rapid and formation of a spinel shell sealed off the molten interior of the inclusion from the nebular gas very soon after the peak temperature was reached and cooling began. The very short time scales (<1 s) indicated for the cooling of B6 are not consistent with a large-scale, nebula-wide heating event and suggest instead a local, transient event, perhaps restricted to the inclusion itself, such as a hypervelocity collision. Diffusion in B6 was fast enough that the liquid followed a normal fractional crystallization sequence, and the TiO_2 content was low enough that $CaAl_4O_7$ formed in the core of the spherule. All other Murchison hibonite-spinel spherules found thus far either contain a sufficient amount of TiO_2 to have significantly expanded the stability field of hibonite relative to $CaAl_4O_7$ and/or cooled quickly enough to have crystallized spinel + hibonite metastably instead of $CaAl_4O_7$. In order for $CaAl_4O_7$ to crystallize from a melt, as occurred in B6, the melt must be very high in Al_2O_3 and low in MgO and TiO_2. For corundum to crystallize, the melt must, in addition, be very low in CaO and have >85 wt% Al_2O_3. Apparently, most condensed corundum continued to react with the solar nebular gas until hibonite, perovskite, and spinel condensed, forming multiphase aggregates, so that most CAIs do not have such extreme compositions. When these aggregates were melted, they gave rise to liquids too rich in TiO_2, MgO, and CaO to yield corundum or $CaAl_4O_7$ upon cooling.

Acknowledgments—We wish to thank A. Hsu for performing the disaggregation, P. Sylvester for performing the density separation, and J. Beckett for numerous helpful discussions, calculations, faxes, and a preprint. The manuscript was reviewed by J. Armstrong, R. Hewins, and T. Ireland, and their efforts are appreciated. This work was supported by funds from the National Aeronautics and Space Administration through grants NAG 9-54 and NAGW-3340 (LG), NAG 9-111 and NAGW-3384 (AMD), and NAG 9-52 and NAGW-3345 (to R. N. Clayton), and funding is gratefully acknowledged.

Editorial handling: J. N. Grossman

REFERENCES

ARMSTRONG J. T., MEEKER G. P., HUNEKE J. C., and WASSERBURG G. J. (1982) The Blue Angel: I. The mineralogy and petrogenesis of a hibonite inclusion from the Murchison meteorite. *Geochim. Cosmochim. Acta* **46,** 575–595.

BAR-MATTHEWS M., HUTCHEON I. D., MACPHERSON G. J., and GROSSMAN L. (1982) A corundum-rich inclusion in the Murchison carbonaceous chondrite. *Geochim. Cosmochim. Acta* **46,** 31–41.

BECKETT J. R. and STOLPER E. (1994) The stability of hibonite, melilite and other aluminous phases in silicate melts: Implications for the origin of hibonite-bearing inclusions from carbonaceous chondrites. *Meteoritics* **29,** 41–65.

BERMAN R. G. (1983) A thermodynamic model for multicomponent melts with application to the system CaO-MgO-Al_2O_3-SiO_2. Ph.D. dissertation, Univ. British Columbia.

BERMAN R. G. and BROWN T. H. (1984) A thermodynamic model for multicomponent melts, with application to the system CaO–Al_2O_3–SiO_2. *Geochim. Cosmochim. Acta* **48,** 661–678.

BISCHOFF A., PALME H., and SPETTEL B. (1987) A37—A coarse-grained, volatile element-poor Ca, Al-rich inclusion with huge Fremdlinge. *Lunar Planet. Sci. XVIII,* pp. 81–82. LPI (abstr.).

BISCHOFF A., BECKERLING W., WEBER D., and ZINNER E. (1992) Calcium-dialuminate-bearing inclusions from the Saharan meteorites Acfer 182, Acfer 087 and El Djouf 001: An ion probe study. *Meteoritics* **27,** 204 (abstr.).

BISCHOFF A., PALME H., SCHULTZ L., WEBER D., WEBER H. W., and SPETTEL B. (1993a) Acfer 182 and paired samples, an iron-rich carbonaceous chondrite: Similarities with ALH85085 and relationship to CR chondrites. *Geochim. Cosmochim. Acta* **57,** 2631–2648.

BISCHOFF A. et al. (1993b) Paired Renazzo-type (CR) carbonaceous chondrites from the Sahara. *Geochim. Cosmochim. Acta* **57,** 1587–1604.

BOYNTON W. V. (1975) Fractionation in the early solar nebula: Condensation of yttrium and the rare earth elements. *Geochim. Cosmochim. Acta* **39,** 569–584.

BOYNTON W. V. and WARK D. A. (1987) Origin of CAI rims—I. The evidence from the rare earth elements. *Lunar Planet. Sci. XVIII,* pp. 117–118. LPI (abstr.).

CATANZARO E. J., MURPHY T. J., GARNER E. L., and SHIELDS W. R. (1966) Absolute isotopic abundance ratios and atomic weights of magnesium. *J. Res. Nat. Bur. Stand.* **70a,** 453–458.

CHAMBERLIN L., BECKETT J. R., and STOLPER E. (1992) Experimental measurement of oxide activities in spinels on the join $MgAl_2O_4$-$Al_{8/3}O_4$ at 1400°C, 1 atm. *GSA Abstr. with Prog.* **24,** A257 (abstr.).

CONARD R. (1976) A study of the chemical composition of Ca-Al-rich inclusions from the Allende meteorite. M.S. thesis, Oregon State Univ.

DAVIS A. M. and GROSSMAN L. (1979) Condensation and fractionation of rare earths in the solar nebula. *Geochim. Cosmochim. Acta* **43,** 1611–1632.

DAVIS A. M., TANAKA T., GROSSMAN L., LEE T., and WASSERBURG G. J. (1982) Chemical composition of HAL, an isotopically-unusual Allende inclusion. *Geochim. Cosmochim. Acta* **46,** 1627–1651.

DAVIS A. M., HASHIMOTO A., CLAYTON R. N., and MAYEDA T. K. (1990) Isotope mass fractionation during evaporation of Mg_2SiO_4. *Nature* **347,** 655–658.

DAVIS A. M. et al. (1991) Melt solidification and late-stage evaporation in the evolution of a FUN inclusion from the Vigarano C3V chondrite. *Geochim. Cosmochim. Acta* **55,** 621–637.

EKAMBARAM V., KAWABE I., TANAKA T., DAVIS A. M., and GROSSMAN L. (1984) Chemical compositions of refractory inclusions in the Murchison C2 chondrite. *Geochim. Cosmochim. Acta* **48,** 2089–2105.

EL GORESY A., PALME H., YABUKI H., NAGEL K., HERRWERTH I., and RAMDOHR P. (1984) A calcium-aluminum-rich inclusion from the Essebi (CM2) chondrite: Evidence for captured spinel-hibonite spherules and for an ultra-refractory rimming sequence. *Geochim. Cosmochim. Acta* **48,** 2283–2298.

FAHEY A. J., GOSWAMI S. N., MCKEEGAN K. D., and ZINNER E. (1987) ^{26}Al, ^{244}Pu, ^{50}Ti, REE, and trace element abundances in hibonite grains from CM and CV meteorites. *Geochim. Cosmochim. Acta* **51,** 329–350.

GEIGER C. A., KLEPPA O. J., MYSEN B. O., LATTIMER J. M., and GROSSMAN L. (1988) Enthalpies of formation of $CaAl_4O_7$ and $CaAl_{12}O_{19}$ (hibonite) by high temperature, alkali borate solution calorimetry. *Geochim. Cosmochim. Acta* **52,** 1729–1736.

GROSSMAN J. N., RUBIN A. E., and MACPHERSON G. J. (1988) ALH85085: a unique volatile-poor carbonaceous chondrite with possible implications for nebular fractionation processes. *Earth Planet. Sci. Lett.* **91,** 33–54.

GROSSMAN L. (1972) Condensation in the primitive solar nebula. *Geochim. Cosmochim. Acta* **36,** 597–619.

GROSSMAN L. (1980) Refractory inclusions in the Allende meteorite. *Ann. Rev. Earth Planet. Sci.* **8,** 559–608.

GROSSMAN L. and GANAPATHY R. (1976) Trace elements in the Allende meteorite—I. Coarse-grained, Ca-rich inclusions. *Geochim. Cosmochim. Acta* **40,** 331–344.

HASHIMOTO A. (1990) Evaporation kinetics of forsterite and implications for the early solar nebula. *Nature* **247,** 53–55.

HINTON R. W. and BISCHOFF A. (1984) Ion microprobe magnesium isotope analysis of plagioclase and hibonite from ordinary chondrites. *Nature* **308,** 169–172.

HINTON R. W., DAVIS A. M., SCATENA-WACHEL D. E., GROSSMAN L., and DRAUS R. (1988) A chemical and isotopic study of hibonite-rich refractory inclusions in primitive meteorites. *Geochim. Cosmochim. Acta* **52,** 2573–2598.

IRELAND T. (1988) Correlated morphological, chemical and isotopic characteristics of hibonites from the Murchison carbonaceous chondrite. *Geochim. Cosmochim. Acta* **52,** 2827–2839.

IRELAND T. R. (1990) Presolar isotopic and chemical signatures in hibonite-bearing refractory inclusions from the Murchison carbonaceous chondrite. *Geochim. Cosmochim. Acta* **54,** 3219–3237.

IRELAND T. R., FAHEY A. J., and ZINNER E. K. (1988) Trace-element abundances in hibonites from the Murchison carbonaceous chondrite: Constraints on high-temperature processes in the solar nebula. *Geochim. Cosmochim. Acta* **52,** 2841–2854.

KEIL K. and FUCHS L. H. (1971) Hibonite [$Ca_2(Al,Ti)_{24}O_{38}$] from the Leoville and Allende chondritic meteorites. *Earth Planet. Sci. Lett.* **12,** 184–190.

KIMURA M., EL GORESY A., PALME H., and ZINNER E. (1993) Ca-Al-rich inclusions in the unique chondrite ALH85085: Petrology, chemistry and isotopic compositions. *Geochim. Cosmochim. Acta* **57,** 2329–2359.

MACDOUGALL J. D. (1981) Refractory spherules in the Murchison meteorite: Are they chondrules? *Geophys. Res. Lett.* **8,** 966–969.

MACPHERSON G. J. and DAVIS A. M. (1994) Refractory inclusions in the type CM chondrite, Mighei. *Geochim. Cosmochim. Acta* (in review).

MACPHERSON G. J., BAR-MATTHEWS M., TANAKA T., OLSEN E., and GROSSMAN L. (1980) Refractory inclusions in Murchison: Recovery and mineralogical description. *Lunar Planet. Sci. XI,* pp. 660–662. LPI (abstr.).

MACPHERSON G. J., GROSSMAN L., ALLEN J. M., and BECKETT J. R. (1981) Origin of rims on coarse-grained inclusions in the Allende meteorite. *Proc. Lunar Planet. Sci. Conf.* **12B,** 1079–1091.

MACPHERSON G. J., BAR-MATTHEWS M., TANAKA T., OLSEN E., and GROSSMAN L. (1983) Refractory inclusions in the Murchison meteorite. *Geochim. Cosmochim. Acta* **47,** 823–839.

MACPHERSON G. J., GROSSMAN L., HASHIMOTO A., BAR-MATTHEWS M., and TANAKA T. (1984a) Petrographic studies of refractory inclusions from the Murchison meteorite. *Proc. 15th Lunar Planet. Sci. Conf., J. Geophys. Res.* **89** (suppl) C299–C312.

MACPHERSON G. J., PAQUE J. M., STOLPER E., and GROSSMAN L. (1984b) The origin and significance of reverse zoning in melilite from Allende Type B inclusions. *J. Geol.* **92,** 289–305.

MACPHERSON G. J., DAVIS A. M., and ZINNER E. K. (1992) Distribution of ^{26}Al in the early solar system—A reappraisal. *Meteoritics* **27,** 253–254 (abstr.).

MICHEL-LÉVY M. C., KURAT G., and BRANDSTÄTTER F. (1982) A new calcium-aluminate from a refractory inclusion in the Leoville carbonaceous chondrite. *Earth Planet. Sci. Lett.* **61,** 13–22.

PAQUE J. M. (1987) $CaAl_4O_7$ from Allende Type A inclusion NMNH4691. *Lunar Planet. Sci. XVIII,* pp. 762–763. LPI (abstr.).

POUCHOU J. L. and PICHOIR F. (1984) A new model for quantitative x-ray microanalysis. Part I: Application to the analysis of homogeneous samples. *Rech. Aerosp. 1984-3,* 13–38.

RICHET P. and BOTTINGA Y. (1980) Heat capacity of liquid silicates: New measurements on $NaAlSi_3O_8$ and $K_2Si_4O_9$. *Geochim. Cosmochim. Acta* **44,** 1535–1541.

SHENG Y. J., WASSERBURG G. J., and HUTCHEON I. D. (1992) Self-diffusion of magnesium in spinel and in equilibrium melts: Constraints on flash heating of silicates. *Geochim. Cosmochim. Acta* **56,** 2535–2546.

SIMON S. B., GROSSMAN L., and DAVIS A. M. (1991) Fassaite composition trends during crystallization of Allende Type B refractory inclusion melts. *Geochim. Cosmochim. Acta* **55,** 2635–2655.

SIMON S. B., GROSSMAN L., and HSU A. (1993a) Petrography and origin of refractory inclusions from the Murray and Murchison C2 chondrites. *Lunar Planet. Sci. XXIV,* pp. 1309–1310. LPI (abstr.).

SIMON S. B., GROSSMAN L., DAVIS A. M., BECKETT J. R., and CHAMBERLIN L. (1993b) Evidence for extremely high-temperature melting in the solar nebula from a $CaAl_4O_7$-bearing spherule from Murchison. *Meteoritics* **28,** 437–438 (abstr.).

STOLPER E. and PAQUE J. M. (1986) Crystallization sequences of Ca-Al-rich inclusions from Allende: The effects of cooling rate and maximum temperature. *Geochim. Cosmochim. Acta* **50,** 1785–1806.

SYLVESTER P. J., GROSSMAN L., and MACPHERSON G. J. (1992) Refractory inclusions with unusual chemical compositions from the Vigarano carbonaceous chondrite. *Geochim. Cosmochim. Acta* **56,** 1343–1363.

SYLVESTER P. J., SIMON S. B., and GROSSMAN L. (1993) Refractory inclusions from the Leoville, Efremovka and Vigarano C3V chondrites: Major element differences between Types A and B, and extraordinary refractory siderophile element compositions. *Geochim. Cosmochim. Acta* **57,** 3763–3784.

VIERTEL H. U. and SEIFERT F. (1980) Thermal stability of defect spinels in the system $MgAl_2O_4$-Al_2O_3. *Neues Jahrb. Mineral.* **140,** 89–101.

WANG J., DAVIS A. M., HASHIMOTO A., and CLAYTON R. N. (1991) The role of diffusion in the isotopic fractionation of magnesium during the evaporation of forsterite. *Lunar Planet. Sci. XXII,* pp. 1461–1462. LPI (abstr.).

WANG J., DAVIS A. M., HASHIMOTO A., and CLAYTON R. N. (1993) Diffusion-controlled isotopic fractionation of a single crystal forsterite evaporated from the solid state. *Lunar Planet. Sci. XXIV,* pp. 1479–1480. LPI (abstr.).

YONEDA S., SYLVESTER P. J., SIMON S. B., GROSSMAN L., and HSU A. (1993) Trace element compositions of spinel-rich refractory inclusions from the Murchison meteorite. *Lunar Planet. Sci. XXIV,* pp. 1563–1564. LPI (abstr.).